

Operational modes of a Raman-coupled two-qubit quantum thermal machine

Alonso Alcalá,¹ Charlie Oncebay,¹ Onofre Rojas,² and Moises Rojas²

¹*Faculty of Sciences, National University of Engineering, 15032 Lima, Peru*

²*Department of Physics, Institute of Natural Science,
Federal University of Lavras, 37200-900 Lavras-MG, Brazil*

We investigate a quantum thermal machine composed of two qubits coupled through a Raman-induced exchange interaction and driven by inhomogeneous transition frequencies. The system is analyzed within Carnot, Otto, and Stirling thermodynamic cycles, including the Stirling cycle with and without regeneration. We identify the conditions under which the device operates as a heat engine, refrigerator, thermal accelerator, or heater. Efficiency maps and operational-mode diagrams reveal well-defined boundaries in parameter space, governed by the frequency ratio $r = \bar{\omega}/\omega$, the coupling strength g , and the thermal gradient between reservoirs. The Carnot cycle exhibits sharp transitions between engine and refrigerator regimes, while the Otto cycle displays a richer structure with the coexistence of all operational modes. The Stirling cycle shows enhanced versatility and performance, particularly when assisted by a regenerator, where near-ideal efficiencies are achieved. Overall, the Raman-type interaction introduces a controllable left-right asymmetry that enables nontrivial manipulation of thermodynamic behavior through frequency tuning.

I. INTRODUCTION

Quantum thermodynamics investigates how familiar thermodynamic laws emerge from quantum dynamics, and how coherence, entanglement and measurement back-action modify energy conversion at the nanoscale [1–5]. This framework raises fundamental questions about the applicability of classical bounds, such as the Carnot limit, and about the extent to which genuinely quantum resources can enhance the performance of engines, refrigerators and related thermal devices [6, 7]. Despite major progress, the field remains conceptually open and continues to expand without a fully unified formulation [8].

Quantum heat machines provide an operational setting in which these issues can be probed. Cyclic protocols based on Hamiltonian modulation and thermal contact have now been implemented in a wide range of platforms. Single trapped ions have demonstrated fully controlled thermodynamic cycles at the level of one particle [9], while ultracold atomic collisions allow heat exchange in quantized energy packets [10]. Nuclear magnetic resonance experiments enable precise manipulation of coupled spins with direct access to work and entropy production [11]. In mesoscopic solid-state devices, quantum dots and nanoelectronic conductors operate near thermodynamic limits [12, 13], and Josephson-based elements support phase-coherent heat transport and thermoelectric effects [14, 15]. Opto- and nanomechanical setups use light-matter interactions or engineered noise to generate refrigeration and heat flow [16, 17]. Circuit quantum electrodynamics (circuit-QED) platforms, with superconducting qubits interacting through microwave resonators, implement autonomous refrigeration as well as measurement-based feedback protocols [18, 19]. These diverse realizations collectively demonstrate that thermodynamic laws can be investigated across many physical settings, each with different degrees of control, noise and scalability.

Within this landscape, interacting spin systems occupy a prominent role as versatile and experimentally accessible working media. Two-qubit Heisenberg engines under static and anisotropic magnetic frequencies have been investigated extensively, including effects of Dzyaloshinskii-Moriya and Kaplan-Shekhtman-Entin-Wohlgemuth-Aharony (KSEA) interactions [20–23]. Multi-spin extensions exploiting XXZ chains, Hubbard-type couplings and controllable double quantum dots have broadened the range of architectures where collective and correlated phenomena appear [24–27]. Spin-based refrigerators and Otto engines have also been studied near critical points to assess the influence of many-body effects and entanglement on performance [28, 29]. Stirling-type spin engines have been shown to benefit from regeneration mechanisms that can approach Carnot efficiency, and from anisotropic couplings that generate richer operational behavior [30–36]. Additional proposals include higher-dimensional lattices, dipolar-coupled nuclear spins and binuclear molecular complexes serving as effective two-spin working media [37–39]. In these settings, entanglement has been examined as a functional resource with consistent thermodynamic interpretation [40, 41].

Despite this extensive literature, most studies rely on symmetric Heisenberg- or Ising-type exchange interactions. In contrast, comparatively less attention has been devoted to left-right asymmetric Raman-type couplings, such as $\sigma_L^z \sigma_R^x$, which arise naturally in ferromagnetic and nuclear-spin environments and can be engineered in platforms including cavity QED, trapped ions, circuit QED and optomechanics [42]. Moreover, the majority of existing works address a single cycle (typically Otto), without a unified comparison across different cycles acting on the same microscopic working substance or a systematic mapping of distinct operating modes heat engine, refrigerator, heater and thermal accelerator, within the same parameter space.

The present work addresses these gaps. We consider a

two-qubit system with Raman-type coupling as a concrete and experimentally motivated platform, and we systematically analyze three standard quantum cycles Carnot, Otto and Stirling (with and without regeneration), under the same Hamiltonian and control scheme. By constructing operational-mode diagrams and performance maps as functions of frequency parameters, we identify the conditions for optimized work extraction or cooling and reveal thermodynamic signatures unique to asymmetric level mixing.

The remainder of the paper is organized as follows. In Sec. II we introduce the Hamiltonian, thermalization processes and the general structure of the quantum cycles. Sec. III describes the operational modes and thermodynamic behavior of the Carnot, Otto and Stirling engines. Sec. IV presents the performance analysis, including efficiency and coefficient-of-performance maps and the role of regeneration. Finally, Sec. V summarizes our main conclusions and discusses its implications.

II. MICROSCOPIC MODEL AND THERMODYNAMIC FRAMEWORK

We consider a system of two interacting qubits with transition frequencies $\bar{\omega}$ and ω , as illustrated in Fig. 1. This model, previously explored as a quantum optical two-atom thermal diode [42], is physically realized by spin-1/2 particles coupled through an anisotropic Raman-type interaction. Throughout this work we set $\hbar = 1$. The system Hamiltonian is given by

$$H = \frac{\bar{\omega}}{2}(\sigma_z \otimes \mathbb{I}) + \frac{\omega}{2}(\mathbb{I} \otimes \sigma_z) + g(\sigma_z \otimes \sigma_x), \quad (1)$$

where σ_x and σ_z are Pauli matrices, $\bar{\omega}$ and ω denote the transition frequencies of the left and right qubits, respectively, and g is the coupling strength associated with the Raman-induced exchange interaction.

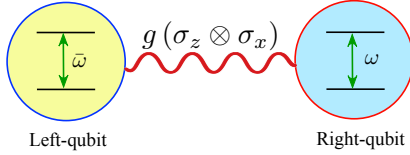


Figure 1. Schematic representation of the Raman-coupled two-qubit system, where the right-qubit transition frequency is externally tuned while the left qubit remains fixed.

In the computational basis $\{|00\rangle, |01\rangle, |10\rangle, |11\rangle\}$, the Hamiltonian can be written in block-diagonal form as

$$H = \begin{pmatrix} H_+ & 0 \\ 0 & H_- \end{pmatrix}, \quad (2)$$

with two 2×2 blocks:

$$H_+ = \begin{pmatrix} \frac{\bar{\omega}+\omega}{2} & g \\ g & \frac{\bar{\omega}-\omega}{2} \end{pmatrix}, \quad (3)$$

$$H_- = \begin{pmatrix} -\frac{\bar{\omega}-\omega}{2} & -g \\ -g & -\frac{\bar{\omega}+\omega}{2} \end{pmatrix}. \quad (4)$$

Diagonalizing these blocks yields four nondegenerate eigenvalues

$$\begin{aligned} E_1 &= \frac{\bar{\omega} + \Omega}{2}, \\ E_2 &= \frac{\bar{\omega} - \Omega}{2}, \\ E_3 &= \frac{-\bar{\omega} + \Omega}{2}, \\ E_4 &= \frac{-\bar{\omega} - \Omega}{2}, \end{aligned} \quad (5)$$

where $\Omega = \sqrt{4g^2 + \omega^2}$.

The corresponding eigenvectors can be written as rotated basis states with a mixing angle θ ,

$$\begin{aligned} |\varphi_1\rangle &= \cos \frac{\theta}{2} |00\rangle + \sin \frac{\theta}{2} |01\rangle, \\ |\varphi_2\rangle &= \sin \frac{\theta}{2} |00\rangle - \cos \frac{\theta}{2} |01\rangle, \\ |\varphi_3\rangle &= \sin \frac{\theta}{2} |10\rangle - \cos \frac{\theta}{2} |11\rangle, \\ |\varphi_4\rangle &= \cos \frac{\theta}{2} |10\rangle + \sin \frac{\theta}{2} |11\rangle, \end{aligned} \quad (6)$$

where the angle satisfies $\tan(\theta) = \frac{2g}{\omega}$.

At thermal equilibrium with a bath at temperature T , the system is described by the Gibbs state

$$\rho(T) = \frac{e^{-\beta H}}{Z} = \sum_{i=1}^4 p_i |\varphi_i\rangle \langle \varphi_i|, \quad (7)$$

where $\beta = 1/(k_B T)$ is the inverse bath temperature and

$$p_i = \frac{e^{-\beta E_i}}{Z}, \quad Z = \sum_{i=1}^4 e^{-\beta E_i} \quad (8)$$

are the thermal populations and partition function, respectively.

Since the Hamiltonian is block-diagonal in the computational basis, the thermal state preserves this structure:

$$\rho(T) = \frac{1}{Z} \begin{pmatrix} \rho^+ & 0 \\ 0 & \rho^- \end{pmatrix}, \quad (9)$$

where ρ^+ acts in the $\{|00\rangle, |01\rangle\}$ subspace and ρ^- in the

$\{|10\rangle, |11\rangle\}$ subspace.

$$\rho_{11}^+ = e^{-\beta\bar{\omega}/2} \left[\cosh\left(\frac{\beta\Omega}{2}\right) - \frac{\omega}{\Omega} \sinh\left(\frac{\beta\Omega}{2}\right) \right], \quad (10)$$

$$\rho_{22}^+ = e^{-\beta\bar{\omega}/2} \left[\cosh\left(\frac{\beta\Omega}{2}\right) + \frac{\omega}{\Omega} \sinh\left(\frac{\beta\Omega}{2}\right) \right], \quad (11)$$

$$\rho_{12}^+ = \rho_{21}^+ = -\frac{2g}{\Omega} e^{-\beta\bar{\omega}/2} \sinh\left(\frac{\beta\Omega}{2}\right), \quad (12)$$

$$\rho_{11}^- = e^{\beta\bar{\omega}/2} \left[\cosh\left(\frac{\beta\Omega}{2}\right) - \frac{\omega}{\Omega} \sinh\left(\frac{\beta\Omega}{2}\right) \right], \quad (13)$$

$$\rho_{22}^- = e^{\beta\bar{\omega}/2} \left[\cosh\left(\frac{\beta\Omega}{2}\right) + \frac{\omega}{\Omega} \sinh\left(\frac{\beta\Omega}{2}\right) \right], \quad (14)$$

$$\rho_{12}^- = \rho_{21}^- = -\frac{2g}{\Omega} e^{\beta\bar{\omega}/2} \sinh\left(\frac{\beta\Omega}{2}\right), \quad (15)$$

These expressions reflect thermally induced coherence within each subspace whenever $\theta \neq 0$, evidencing the role of the Raman-type interaction in mixing basis states even at equilibrium.

A. Internal energy and entropy

The thermodynamic properties of the system follow directly from the Gibbs state in Eq. (8). The internal energy is defined as

$$U = \text{Tr}\{\rho H\} = \sum_{i=1}^4 p_i E_i, \quad (16)$$

where E_i and p_i are given in Eqs. (5) and (9), respectively. The von Neumann entropy of the thermal state is

$$\mathcal{S} = -\text{Tr}\{\rho \ln \rho\} = -k_B \sum_{i=1}^4 p_i \ln p_i. \quad (17)$$

Since the spectrum depends on the control parameters $(\bar{\omega}, \omega, g)$, variations of these quantities change the internal energy according to

$$dU = \sum_{i=1}^4 E_i dp_i + \sum_{i=1}^4 p_i dE_i. \quad (18)$$

The first term accounts for population changes and corresponds to energy exchange with the environment (heat). The second term stems from modifications of the Hamiltonian eigenvalues and is associated with the work performed on or by the system. This leads to the standard decomposition used in quantum thermodynamics,

$$dU = \delta Q + \delta W, \quad (19)$$

where

$$\delta Q = \sum_i E_i dp_i, \quad \delta W = \sum_i p_i dE_i. \quad (20)$$

When the system remains in equilibrium with a bath at temperature T during a quasistatic transformation, the entropy change satisfies the Clausius relation $d\mathcal{S} = \beta \delta Q$, ensuring full thermodynamic consistency with the first and second laws.

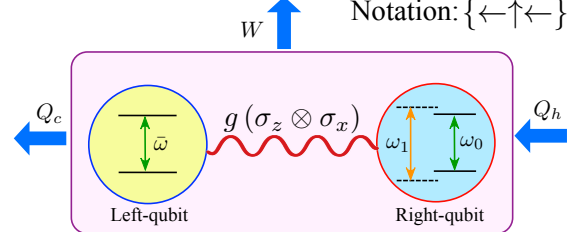


Figure 2. Visual depiction of the two-qubit working substance, where work is produced by tuning the right-qubit transition frequency from ω_0 to ω_1 .

B. Thermodynamic strokes

Quantum thermal machines operate through sequences of quasistatic transformations, in which either the Hamiltonian parameters or the environmental conditions are externally controlled. The working substance is a two-qubit system, schematically illustrated in Fig. 2. In this setup, useful work is generated by tuning the transition frequencies of the right and left qubits, while heat arises from population changes induced by thermal contact with the reservoirs. Based on the decomposition introduced in Eq. 19, the relevant thermodynamic strokes are defined as follows.

a. Isothermal process The system is weakly coupled to a thermal reservoir at fixed temperature T . As the transition frequency is varied quasistatically, the state remains Gibbsian, and both heat and work are exchanged according to Eq. (19). The entropy increases or decreases depending on whether heat is absorbed from or released to the reservoir.

b. Constant-frequency (isochoric) process The transition frequencies are kept fixed, so that all energy eigenvalues remain constant ($dE_i = 0$). As a result, no work is performed, $\delta W = 0$. Heat exchange with the reservoir drives the populations toward the corresponding thermal distribution, in accordance with Eq. (20).

c. Adiabatic process The system is isolated from the thermal reservoirs, and the evolution is quasistatic, so that the instantaneous eigenstate populations remain fixed ($dp_i = 0$). Consequently, no heat is exchanged, $\delta Q = 0$, and Eq. (20) reduces to $dU = \sum_i p_i dE_i$.

The von Neumann entropy remains constant throughout the stroke. This condition is intrinsically quantum:

| Mode | Q_c | W | Q_h | Scheme | COP |
|--------------|-------|-----|-------|--|------------------------|
| Engine | — | + | + | { $\leftarrow\uparrow\leftarrow\rightarrow$ } | $\eta = \frac{W}{Q_h}$ |
| Refrigerator | + | — | — | { $\rightarrow\downarrow\rightarrow$ } | $\frac{Q_h}{W}$ |
| Heater | — | — | — | { $\leftarrow\downarrow\rightarrow\rightarrow$ } | $\frac{Q_c}{W}$ |
| Accelerator | — | — | + | { $\leftarrow\downarrow\leftarrow\rightarrow$ } | $\frac{Q_c}{W}$ |

Table I. Sign conventions for the cold-bath heat Q_c , net work W , and hot-bath heat Q_h corresponding to the different operational modes of the thermal machine.

suppressing diabatic transitions requires sufficiently slow modulation of the transition frequencies ($\bar{\omega}, \omega$).

C. Conditions modes

When the system operates between a hot reservoir at temperature T_h and a cold reservoir at temperature T_c , the net heat exchanged with each bath and the total work performed over a complete cycle satisfy $W = Q_h + Q_c$, together with the Clausius inequality

$$\oint \frac{\delta Q}{T} \leq 0, \quad (21)$$

which restricts the physically admissible sign combinations of (Q_h, Q_c, W) . As a consequence, only four distinct operation modes are allowed: heat engine, refrigerator, thermal accelerator, and heater. Their sign conventions and thermodynamic interpretation are summarized in Table I.

The boundaries between these regimes depend on the transition frequencies ($\bar{\omega}, \omega$), the coupling strength g , and the temperature difference between the reservoirs. Mapping these boundaries in parameter space constitutes the main objective of the analysis presented in Sec. IV.

D. Performance measures

In the heat engine regime, the performance is quantified by the thermal efficiency

$$\eta = \frac{W}{Q_h}, \quad 0 \leq \eta < 1. \quad (22)$$

This quantity is bound by the second law and depends on the particular sequence of thermodynamic strokes that form the cycle.

For the refrigerator, heater, and accelerator regimes, the most natural metric is the coefficient of performance (COP), which may exceed unity. To enable a direct comparison among all operational modes with a single bounded parameter, we define the normalized performance parameter [25]

$$\kappa = \frac{\text{COP}}{1 + \text{COP}}, \quad 0 < \kappa < 1, \quad (23)$$

which increases monotonically with efficiency. The limits of κ provide a clear interpretation of performance: values near zero indicate poor conversion efficiency, while values close to one correspond to nearly ideal thermodynamic operation. This unified characterization will be employed throughout our analysis of the Carnot, Otto, and Stirling cycles in Sec. III and Sec. IV.

III. QUANTUM THERMODYNAMIC CYCLES

The quantum Carnot, Otto, and Stirling cycles investigated in this study consist of quasistatic stages, as described in Sec. II B. In these cycles, useful work is generated through the modulation of the qubit transition frequencies. Specifically, the cycle is driven by varying the frequency ω of the right qubit, while the frequency $\bar{\omega}$ of the left qubit is determined by the fixed ratio $r = \bar{\omega}/\omega$. This ratio quantifies the spectral asymmetry of the system, with $r = 1$ corresponding to the symmetric configuration. Throughout this analysis, the frequency ω of the right qubit is varied between ω_0 and ω_1 . Heat exchanged occurs via the redistribution of energy-level populations during the thermal contact stages. The overall performance of each cycle depends on both the sequence of these stages and the possibility of internal heat recovery.

The following subsections summarize the structure of each cycle and provide the basis for the operational maps presented in Sec. IV.

A. Carnot cycle

The Carnot cycle consists of two isothermal and two adiabatic strokes. Throughout the cycle, the right-qubit frequency is varied quasistatically between ω_0 and ω_1 .

All thermodynamic quantities are expressed in terms of the instantaneous eigenvalues $E_i(\omega)$ and the corresponding thermal populations $p_i(T, \omega)$. The cycle is initiated from the equilibrium state at (T_c, ω_0) , with populations $p_i^{(0)} = p_i(T_c, \omega_0)$.

a. *Hot isothermal stroke* ($\omega_0 \rightarrow \omega_1, T = T_h$): With the system in contact with the hot reservoir, the frequency is swept from ω_0 to ω_1 . The state remains Gibbsian at temperature T_h with final populations $p_i^{(h)} = p_i(T_h, \omega_1)$. The heat absorbed from the hot bath follows from the entropy change along the isotherm:

$$Q_h = T_h [S(\omega_1, T_h) - S(\omega_0, T_h)]. \quad (24)$$

Work is done through the variation of $E_i(\omega)$, but no explicit formula is needed here since the Carnot efficiency is independent of spectrum details.

b. *Adiabatic expansion* ($\omega_1 \rightarrow \omega_2$): The system is isolated and the frequency changes from ω_1 to ω_2 . The populations remain fixed at $p_i^{(h)}$ while the eigenvalues

change, so

$$Q_2 = 0, \quad W_2 = \sum_i p_i^{(h)} [E_i(\omega_2) - E_i(\omega_1)]. \quad (25)$$

This stroke preserves the entropy of the working medium.

c. *Cold isothermal stroke* ($\omega_2 \rightarrow \omega_3$, $T = T_c$): Coupled to the cold bath at T_c , the system returns to Gibbs equilibrium as the frequency changes from ω_2 to ω_3 . The heat released is

$$Q_c = T_c [S(\omega_3, T_c) - S(\omega_2, T_c)], \quad (26)$$

which is negative for an operating heat engine. Work is again associated with the spectral variation.

d. *Adiabatic compression* ($\omega_3 \rightarrow \omega_0$): In the final stroke the system is isolated and the frequency is returned to its initial value ω_0 , with populations fixed at those of the cold isotherm:

$$Q_4 = 0, \quad W_4 = \sum_i p_i^{(c)} [E_i(\omega_0) - E_i(\omega_3)]. \quad (27)$$

The state returns to $p_i^{(0)}$, closing the cycle.

e. *Work and efficiency*: The total work is $W = Q_h + Q_c$. Under the quasistatic assumptions used in this section, the efficiency attains its standard Carnot form, $\eta_{\text{Carnot}} = 1 - \frac{T_c}{T_h}$, independent of the detailed spectral structure of the Raman-coupled two-qubit system. The feasibility of engine or refrigeration operation for given (ω_0, ω_1) depends instead on the signs of the entropy changes in the two isothermal strokes, as analyzed in Sec. IV.

B. Quantum Otto cycle

The Otto cycle consists of two adiabatic strokes and two constant-frequency strokes. Analogously, the transition frequency of the right qubit is varied quasistatically between ω_0 and ω_1 .

The cycle starts from thermal equilibrium at (T_c, ω_0) , with populations $p_i^{(0)} = p_i(T_c, \omega_0)$.

a. *First adiabatic stroke* ($\omega_0 \rightarrow \omega_1$): The system is isolated and the right-qubit frequency is changed from ω_0 to ω_1 . The populations remain fixed at $p_i^{(0)}$, so this stroke exchanges only work

$$Q_1 = 0, \quad W_1 = \sum_i p_i^{(0)} [E_i(\omega_1) - E_i(\omega_0)]. \quad (28)$$

b. *Hot constant-frequency stroke at ω_1* : With the frequency fixed at ω_1 , the system is brought into contact with the hot reservoir at temperature T_h and relaxes to the Gibbs state with populations $p_i^{(h)} = p_i(T_h, \omega_1)$. Since the spectrum does not change, this stroke exchanges only heat,

$$W_2 = 0, \quad Q_h = \sum_i E_i(\omega_1) [p_i^{(h)} - p_i^{(0)}]. \quad (29)$$

c. *Second adiabatic stroke* ($\omega_1 \rightarrow \omega_0$): The system is again isolated and the frequency is returned from ω_1 to ω_0 . The populations remain equal to $p_i^{(h)}$, so

$$Q_3 = 0, \quad W_3 = \sum_i p_i^{(h)} [E_i(\omega_0) - E_i(\omega_1)]. \quad (30)$$

d. *Cold constant-frequency stroke at ω_0* : Finally, at fixed frequency ω_0 the system is coupled back to the cold reservoir at T_c and relaxes from $p_i^{(h)}$ to the initial populations $p_i^{(0)}$. This stroke exchanges only heat,

$$W_4 = 0, \quad Q_c = \sum_i E_i(\omega_0) [p_i^{(0)} - p_i^{(h)}]. \quad (31)$$

The net work and the first law follow directly,

$$W = W_1 + W_3 = Q_h + Q_c, \quad (32)$$

and the efficiency in engine mode is

$$\eta_{\text{Otto}} = 1 - \frac{|Q_c|}{Q_h}, \quad (33)$$

with all dependence on the control parameters entering through the eigenvalues $E_i(\omega)$ and the thermal populations $p_i(T, \omega)$. This structure underlies the operational maps and performance diagrams in the (ω_0, ω_1) plane discussed in Sec. IV.

C. Quantum Stirling cycle

The Stirling protocol consists of two isothermal processes and two constant-frequency processes. As in the previous cycles, the frequency of the right qubit is modulated between the values ω_0 and ω_1 .

We first consider the conventional Stirling cycle without regeneration, followed by its regenerated version.

1. Stirling cycle without regeneration

The cycle begins at (T_h, ω_0) with equilibrium populations $p_i^{(h,0)} = p_i(T_h, \omega_0)$.

a. *Hot isothermal stroke* ($\omega_0 \rightarrow \omega_1, T = T_h$): The system is in contact with the hot bath while the frequency changes from ω_0 to ω_1 . The state remains Gibbsian with populations $p_i^{(h,1)} = p_i(T_h, \omega_1)$. The heat absorbed is

$$Q_h = T_h [S(\omega_1, T_h) - S(\omega_0, T_h)]. \quad (34)$$

Work is generated through the variation of the eigenvalues.

b. *First constant-frequency stroke at ω_1* : The coupling to the thermal reservoir is then switched to the lower temperature T_c , while the frequency is kept fixed at ω_1 . Since no spectral variation occurs during this stage, the process takes place at constant frequency. No work

is performed, and heat is released during this process, denoted by Q_2

$$Q_2 = \sum_i E_i(\omega_1) [p_i^{(c,1)} - p_i^{(h,1)}], \quad (35)$$

where $p_i^{(c,1)} = p_i(T_c, \omega_1)$ and $p_i^{(h,1)} = p_i(T_h, \omega_1)$.

c. *Cold isothermal stroke* ($\omega_1 \rightarrow \omega_0, T = T_c$): The frequency is slowly returned from ω_1 to ω_0 while the system thermalizes at T_c . The heat released is

$$Q_c = T_c [S(\omega_0, T_c) - S(\omega_1, T_c)] < 0. \quad (36)$$

d. *Second constant-frequency stroke at ω_0* : With the frequency fixed at ω_0 , the system completes its relaxation back to $p_i^{(h,0)}$. As in the first constant-frequency stroke, no spectral work is performed. The heat exchanged during this process is given by

$$Q_4 = \sum_i E_i(\omega_0) [p_i^{(h,0)} - p_i^{(c,0)}], \quad (37)$$

where $p_i^{(c,0)} = p_i(T_c, \omega_0)$. This final thermodynamic stroke simply restores the system to its initial state.

e. *Work and efficiency*: The total work per cycle is

$$W = Q_{in} + Q_{out}, \quad (38)$$

where $Q_{in} = Q_h + Q_4$ and $Q_{out} = Q_2 + Q_c$ and the Stirling efficiency follows from

$$\eta_{St} = \frac{W}{Q_h + Q_4}. \quad (39)$$

Because one of the two non-isothermal strokes is constant-frequency with no spectral contribution, the achievable efficiency depends sensitively on the entropy changes along the two isothermal legs, this dependence is reflected in the operational maps of Sec. IV.

2. Stirling cycle with regeneration

In the regenerated Stirling cycle, the sequence of thermodynamic strokes is identical to that of the standard Stirling machine. However, during the two constant-frequency strokes, heat is no longer exchanged with external reservoirs. Instead, the heat released in the first constant-frequency process is stored internally by the regenerator and subsequently reused in the second one, thereby suppressing external dissipation and enhancing the reversibility of the cycle. The heats associated with the two isochoric strokes at ω_1 and ω_0 are denoted by Q_2 and Q_4 , respectively, and their net contribution is

$$\Delta Q = Q_2 + Q_4. \quad (40)$$

As a consequence, the presence of the regenerator modifies the amount of heat effectively absorbed from the hot reservoir. The total heat input per cycle is then given by

$$Q_{in}^{reg} = Q_h + \delta \Delta Q. \quad (41)$$

where Q_h is the heat absorbed during the hot isothermal stroke and $\delta = 1$ if $\Delta Q > 0$, and $\delta = 0$ if $\Delta Q < 0$. In the following, we restrict our analysis to the case $\Delta Q > 0$, for which the regenerator effectively supplies heat to the cycle. When $\Delta Q < 0$, the regenerator would instead require an additional heat input from the hot reservoir, offering no thermodynamic advantage and reducing the overall efficiency of the engine.

a. *Work and efficiency*: The total output remains

$$W = Q_{in} + Q_{out}. \quad (42)$$

with $Q_{out} = Q_2 + Q_c$, and the efficiency of the Stirling engine with regenerator is correspondingly defined as

$$\eta_{St}^{reg} = \frac{W}{Q_{in}^{reg}}. \quad (43)$$

Due to the internal recovery of heat provided by the regenerator, the efficiency approaches its ideal limit. This mechanism accounts for the high-efficiency regions observed in the operational maps of the regenerated Stirling cycle presented in Sec. IV.

IV. RESULTS AND DISCUSSIONS

In this section, we investigate the operational modes and performance of a Raman-coupled two-qubit system. The thermodynamic cycles are driven by modulating the frequency ω of the right qubit, which is varied between ω_0 and ω_1 . The parameter r characterizes the spectral asymmetry of the system, with $r = 1$ corresponding to the symmetric configuration.

A. Operational-mode diagrams

For fixed temperatures and coupling, the Raman interaction and the inhomogeneous frequencies transition (ω_0, ω_1) control the level structure and, consequently, the regions where the cycle behaves as an engine, refrigerator, heater, or accelerator. Figures 3 to 6 display these modes for the Carnot, Otto, and Stirling cycles, with and without regenerator, and illustrate how the choice of protocol reshapes the operational boundaries in the (ω_0, ω_1) plane.

1. Quantum Carnot cycle

Figure 3 shows the operational-mode diagrams of the quantum Carnot cycle in the (ω_0, ω_1) plane. Here, ω_0 and ω_1 denote the two values of the right-qubit frequency used during the adiabatic strokes, while the left-qubit

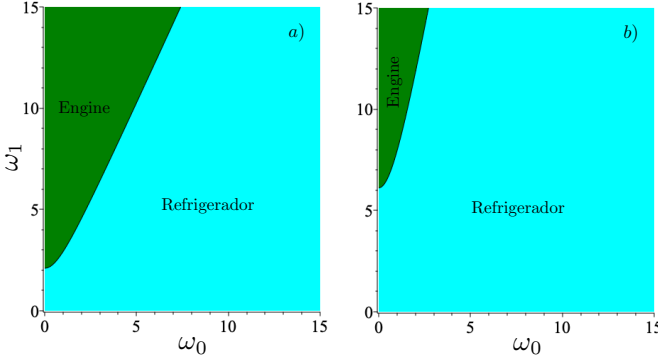


Figure 3. Schematic representation of Quantum Carnot machine cycle in the $\omega_0 - \omega_1$ plane. a) For $T_c = 1$, and $T_h = 2$. b) For $T_c = 1$, and $T_h = 5$. The parameters are set to $r = 1$, and $g = 1$.

frequency is kept fixed. The colored regions indicate whether the machine operates as a heat engine or as a refrigerator.

In panel 3(a) the reservoir temperatures are $T_c = 1$ and $T_h = 2$. Two distinct operating domains are clearly visible. The green region corresponds to engine operation, where positive work is extracted from the temperature difference between the baths. The cyan region represents the refrigerator regime, in which external work is required to transfer heat from the cold reservoir to the hot one. The curve separating these regions corresponds to the condition of zero net work over a complete cycle.

Panel 3(b) displays the same cycle for a stronger thermal gradient, with $T_c = 1$ and $T_h = 5$. In this case the heat-engine region becomes narrower and shifts toward lower values of ω_0 , while the refrigeration domain expands and occupies most of the (ω_0, ω_1) plane. This shows that, although the Carnot efficiency increases with the ratio T_h/T_c , the set of frequency parameters that support reversible work extraction becomes more restricted when the temperature difference is large.

In summary, the Carnot cycle attains the maximal theoretical efficiency wherever it operates as a heat engine, but the strict reversibility conditions confine this regime to a relatively small region.

2. Quantum Otto cycle

Figure 4 shows the operational-mode diagrams of the quantum Otto cycle in the (ω_0, ω_1) plane. The colors distinguish heat engine (green), refrigerator (cyan), thermal accelerator (red), and heater (yellow) behavior. In all cases, the frequency applied to the right-qubit is modulated between ω_0 and ω_1 , while the frequency on the left-qubit is fixed.

In panel 4(a), with $T_c = 1$, $T_h = 2$, and $r = 1$, the heat-engine mode dominates the sector $\omega_1 > \omega_0$, where the expansion stroke enhances the level spacing and allows positive work extraction. A refrigerator region also ap-

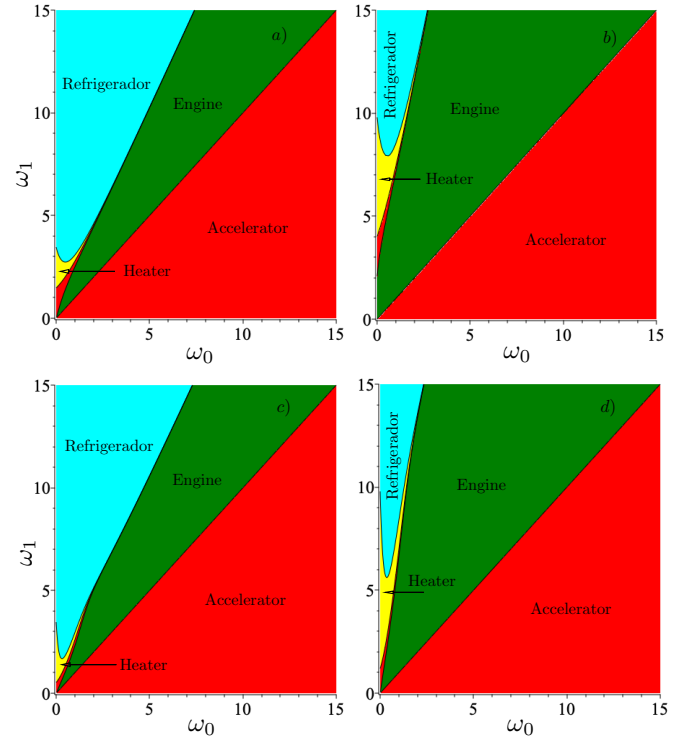


Figure 4. Operational modes of the quantum Otto cycle in the $\omega_0 - \omega_1$ plane for different parameter configurations. a) $r = 1$, $T_c = 1$, and $T_h = 2$. b) $r = 1$, $T_c = 1$, and $T_h = 5$. c) $r = 3$, $T_c = 1$, and $T_h = 2$. d) $r = 3$, $T_c = 1$, and $T_h = 5$. The coupling parameter was fixed at $g = 1$.

pears in the same quadrant, but only for sufficiently large frequencies $\omega_1 \gtrsim 2.8$, indicating that cooling requires a minimum spectral response to thermalization. Thin heater and accelerator bands reflect parameter ranges where spectral reshaping and reservoir imbalance do not align favorably with work extraction.

The effect of increasing the thermal gradient is shown in panel 4(b), for $T_h = 5$. The engine region expands significantly and extends to larger frequency values, demonstrating that stronger thermal biases enhance work output. In contrast, refrigeration becomes restricted to very large values of ω_1 , meaning that cooling operation is increasingly suppressed. Heater regions become more visible, signaling stronger irreversibility under large temperature imbalance.

Panels 4(c) and (d) illustrate the impact of spectral asymmetry for $r = 3$. For $T_h = 2$ [panel c], the refrigeration region expands, confirming that stronger compression enhances population redistribution and, consequently, heat extraction from the cold reservoir. The accelerator region is reduced, indicating that asymmetry suppresses inefficient work-assisted conduction. When both effects are combined, $T_h = 5$ and $r = 3$ in Fig. 4(d), the heat engine remains the dominant operational mode in $\omega_1 > \omega_0$, while the refrigerator window becomes narrow and heater behavior becomes more prominent near

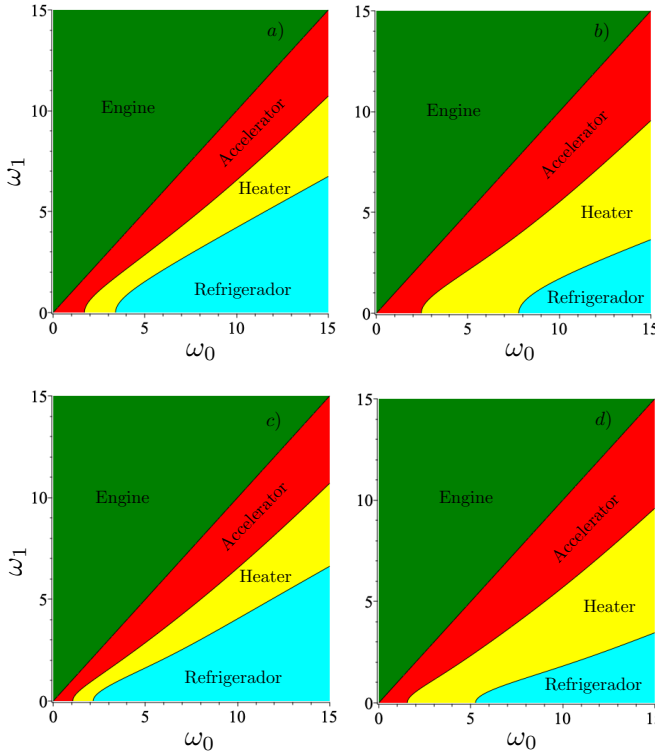


Figure 5. Operational modes of the quantum Stirling cycle in the $\omega_0 - \omega_1$ plane for different parameter configurations. a) $r = 1$, $T_c = 1$, and $T_h = 2$. b) $r = 1$, $T_c = 1$, and $T_h = 3$. c) $r = 2$, $T_c = 1$, and $T_h = 2$. d) $r = 2$, $T_c = 1$, and $T_h = 3$. The coupling parameter was fixed at $g = 1$.

the boundaries between regimes.

Overall, the Otto cycle exhibits a rich thermodynamic structure, with its operational landscape controlled by the interplay between thermal gradient and frequency asymmetry. Larger T_h/T_c favors engine performance, whereas stronger compression enhances refrigeration. Accelerator and heater modes persist only in regions where the spectral response to the stroke is insufficient to support efficient thermodynamic conversion.

3. Stirling Cycle

The Stirling protocol combines two isothermal and two constant-frequency strokes, and its operational modes depend crucially on whether a regenerator is present. Figure 5 depicts the mode diagram without regeneration, while Fig. 6 shows the corresponding behavior when an ideal regenerator is included. In both cases the coupling is fixed at $g = 1$, and different panels explore the effect of temperature gradient and frequency ratio.

a. Operation without regenerator Figure 5 presents the operational-mode diagrams of the Stirling cycle in the (ω_0, ω_1) plane. Four operating regimes are observed: heat engine (green), refrigerator (cyan), thermal accelerator (red), and heater (yellow).

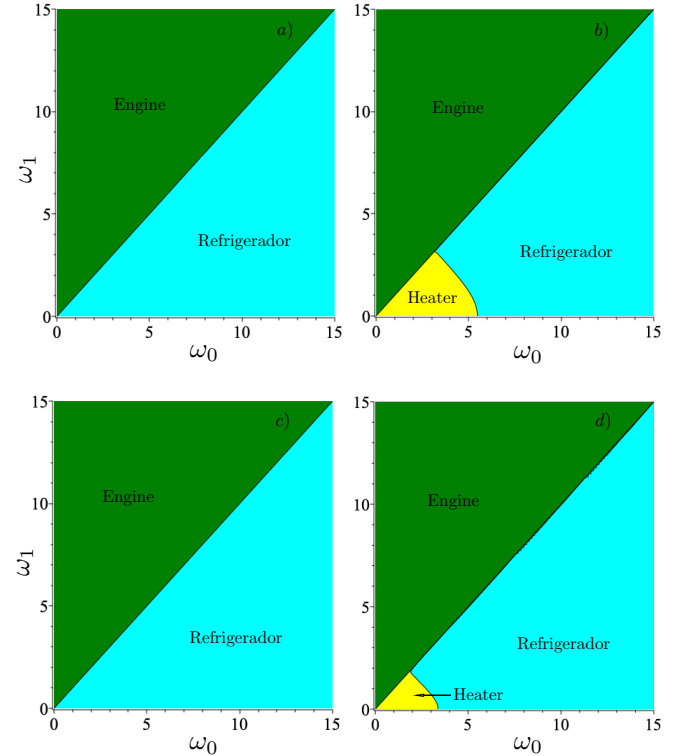


Figure 6. Operational modes of the quantum Stirling cycle with a regenerator in the $\omega_0 - \omega_1$ plane for different parameter configurations. a) $r = 1$, $T_c = 1$, and $T_h = 2$. b) $r = 1$, $T_c = 1$, and $T_h = 3$. c) $r = 2$, $T_c = 1$, and $T_h = 2$. d) $r = 2$, $T_c = 1$, and $T_h = 3$. The coupling parameter was fixed at $g = 1$.

In panels 5(a) and (b), the parameters are fixed at $g = 1$, $r = 1$, and $T_c = 1$. For moderate thermal bias, $T_h = 2$ [panel 5(a)], cooling operation requires sufficiently large frequencies with $\omega_0 > \omega_1$ and $\omega_0 \gtrsim 3.5$. Increasing the thermal gradient to $T_h = 3$ [panel 5(b)] shifts the onset of refrigeration to significantly larger values of ω_0 , while heater behavior expands near the boundaries. In both cases, engine operation dominates for $\omega_1 > \omega_0$, where the stroke increases the hybridized energy gap.

Panels 5(c) and (d) illustrate the effect of spectral asymmetry for $r = 2$. For $T_h = 2$ [panel 5(c)], refrigeration becomes accessible at lower frequencies, $\omega_0 \gtrsim 2.1$, showing that stronger compression improves heat extraction from the cold bath. When $T_h = 3$ [panel 5(d)], refrigeration again shifts to larger ω_0 , accompanied by a broader heater region. Overall, without regeneration the Stirling cycle displays a strong dependence on the thermal gradient, and refrigeration is only achievable when the spectral response to the isothermal strokes is sufficiently large.

b. Operation with regenerator Figure 6 displays the operational maps of the Stirling cycle when a regenerator is included. The presence of the regenerator eliminates the constant-frequency heat exchange with the reservoirs, ensuring that heat transfer occurs only dur-

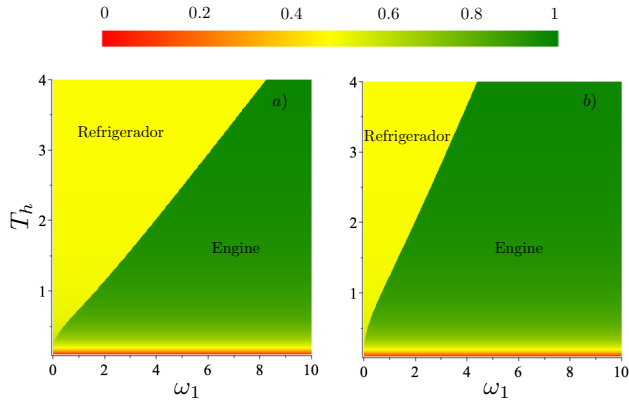


Figure 7. Normalized Carnot performance in the $\omega_1 - T_h$ plane. a) $r = 1$. b) $r = 3$. The parameters are fixed at $T_c = 0.1$, $\omega_0 = 0$, and $g = 1$.

ing the isothermal strokes. In panel 6(a), for $r = 1$, $T_c = 1$, and $T_h = 2$, only heat-engine and refrigerator modes are present. The boundary between them coincides with the line $\omega_0 = \omega_1$. The absence of heater and accelerator regions indicates that regeneration avoids dissipation into both reservoirs. Increasing the thermal gradient to $T_h = 3$ [panel 6(b)] produces a small heater region for $\omega_0 > \omega_1$ and small frequencies, reflecting the onset of irreversibility when the input heat exceeds what can be stored and reused internally. When effect of spectral asymmetry is increased to $r = 2$ [panel 6(c)], the heater region is suppressed again and only engine and refrigerator modes remain accessible, showing that compression compensates for the thermal imbalance.

Finally, in panel 6(d), combining $r = 2$ and $T_h = 3$ reintroduces a narrow heater strip near small ω_0 . Even so, the operational boundaries between engine and refrigerator modes remain nearly unchanged. This demonstrates that regeneration stabilizes Stirling operation and strongly reduces dissipative behavior, even under large frequency asymmetry and pronounced temperature bias.

B. Efficiency and COP maps

While the operational-mode diagrams identify where a cycle functions as engine or refrigerator, the performance inside each region depends on how effectively frequency modulation reshapes the energy spectrum relative to the thermal gradient. Figures 7-10 display the efficiency for the Carnot and Otto cycles, and the normalized coefficient of performance κ for the Stirling protocols, across the (ω_0, ω_1) parameter plane. These maps reveal how the Raman-induced spectral sensitivity governs the conversion of thermal resources into useful work or cooling power.

1. Carnot efficiency

Figure 7 shows the normalized Carnot performance in the (ω_1, T_h) plane for two values of frequency asymmetry. The normalization ensures that $\kappa = 1$ corresponds to the ideal Carnot efficiency $1 - T_c/T_h$, while $\kappa = 0$ indicates vanishing efficiency or COP. For $r = 1$ [panel 7(a)], the operation is divided into heat engine and refrigerator regions. The engine mode displays consistently high efficiency, with $\kappa \approx 0.9$ across a broad range of T_h , indicating that frequency modulation is well aligned with entropy reshaping during the isothermals. The refrigerator domain exhibits more moderate performance, $\kappa \approx 0.5$, and is confined to smaller values of ω_1 and T_h . When the spectral asymmetry increases to $r = 3$ [panel 7(b)], the qualitative structure remains the same, but the engine region expands while the refrigerator domain becomes narrower. This indicates that a stronger compression ratio facilitates work extraction even for weaker frequency strokes. In both cases, the contour lines remain almost horizontal, showing that the Carnot performance is controlled predominantly by the thermal gradient and is only weakly sensitive to the absolute frequency value within the parameter range considered.

Overall, the Carnot protocol demonstrates that whenever engine operation is thermodynamically allowed, it proceeds with efficiency close to the reversible bound. The main limitation stems from progressive shrinking of the admissible operation region as the frequency ratio or the thermal asymmetry increases.

2. Otto efficiency

Figure 8 shows the normalized performance κ of the Otto cycle in the (ω_0, ω_1) plane for different thermal gradients and frequency asymmetry. For heat-engine operation, κ coincides with the thermodynamic efficiency η . In the refrigerator, heater, and accelerator modes, κ corresponds to the normalized COP, enabling direct comparison across all regimes.

For $r = 1$ and $T_h = 2$ [panel 8(a)], the heat-engine regime dominates the sector $\omega_1 > \omega_0$, where the expansion stroke increases the level splitting. Performance is modest, $\eta \lesssim 0.5$, but increases near the boundary with the refrigerator region, reflecting enhanced thermodynamic response at the onset of cooling operation. Refrigeration requires sufficiently strong hybridization and appears only at larger frequencies. Accelerator and heater modes remain confined to small pockets where the direction of spectral reshaping does not align with the thermal bias.

A stronger thermal gradient, $T_h = 5$ [panel 8(b)], substantially expands the engine region, boosting efficiency up to $\eta \approx 0.8$, while refrigeration becomes restricted to very large ω_1 . This indicates that strong temperature bias favors work extraction but makes cooling more difficult. Heater behavior increases near the operational

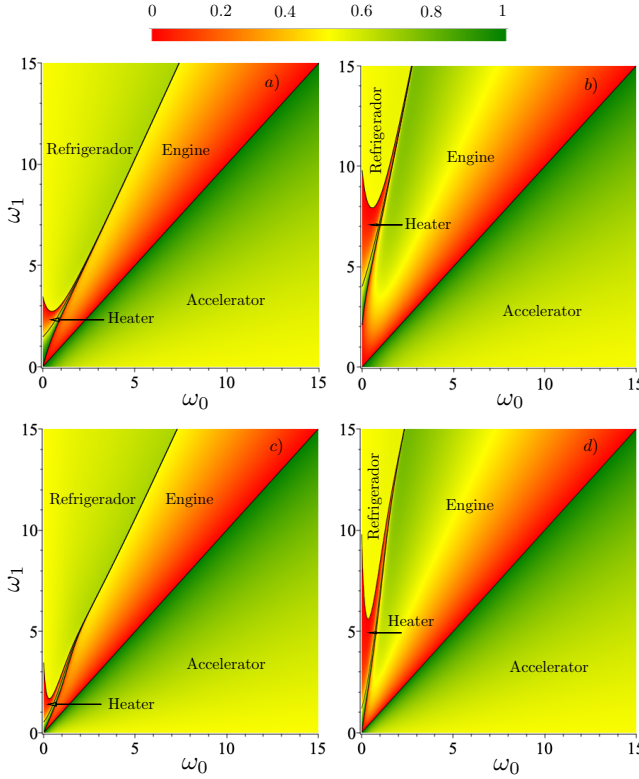


Figure 8. Thermal efficiency of the quantum Otto cycle in the ω_0 - ω_1 plane. a) $r = 1$, $T_c = 1$, and $T_h = 2$. b) $r = 1$, $T_c = 1$, and $T_h = 5$. c) $r = 3$, $T_c = 1$, and $T_h = 2$. d) $r = 3$, $T_c = 1$, and $T_h = 5$. The coupling parameter was fixed at $g = 1$.

boundaries due to growing irreversibility.

Panels 8(c) and (d) show the effect of spectral asymmetry, $r = 3$. At moderate thermal bias [$T_h = 2$, panel 8(c)], refrigeration expands toward lower frequencies, demonstrating that compression enhances population reshaping and enables more efficient cooling. Heater operation is significantly suppressed. When both parameters are large, $r = 3$ and $T_h = 5$ [panel 8(d)], the heat-engine region remains dominant with high performance, while refrigeration is confined to a narrow strip at large frequencies, while heater regions become more pronounced near the low-frequency boundaries, where the coefficient κ attains small values.

In summary, Otto performance is governed by the interplay between spectral reshaping and thermal bias: increasing T_h/T_c favors work extraction, whereas increasing r favors refrigeration. Accelerator and heater behavior appear when neither condition is sufficiently met for efficient operation.

3. Stirling cycles with and without regeneration

Figures 9 and 10 present the performance maps of the Stirling cycle, without and with an ideal regeneration process included. These diagrams reveal that Stirling

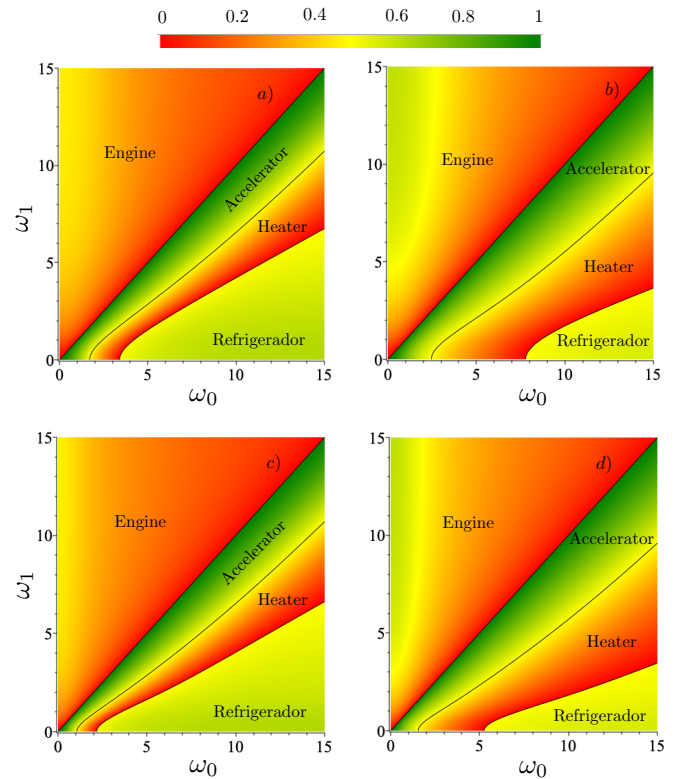


Figure 9. Thermal efficiency of the quantum Stirling cycle in the ω_0 - ω_1 plane. a) $r = 1$, $T_c = 1$, and $T_h = 2$. b) $r = 1$, $T_c = 1$, and $T_h = 3$. c) $r = 2$, $T_c = 1$, and $T_h = 2$. d) $r = 2$, $T_c = 1$, and $T_h = 3$. The coupling parameter was fixed at $g = 1$.

behavior is governed primarily by how efficiently thermal population reshaping is exploited during the two isothermal strokes and how much heat is lost during the constant-frequency branches.

a. Stirling without regeneration Figure 9 shows the normalized performance κ of the Stirling cycle without regeneration in the (ω_0, ω_1) plane. As in the Otto case, κ equals the engine efficiency in the $\omega_1 > \omega_0$ region and represents the normalized COP in the refrigerator and accelerator regimes. For $g = 1$, $r = 1$, and $T_h = 2$ [panel 9(a)], engine operation dominates for $\omega_1 > \omega_0$ with moderate performance $\eta \approx 0.5$. Refrigeration is only feasible for larger ω_0 , where hybridization is strong enough to support heat extraction. Accelerator behavior exhibits high κ values due to large entropy reshaping under quasi-degenerate conditions, whereas the heater mode remains inefficient. Raising the thermal gradient to $T_h = 3$ [panel 9(b)] enhances the engine efficiency and shifts refrigeration to higher ω_0 . Heater regions expand because dissipation increases when the internal heat released during the constant-frequency strokes is dumped directly into the baths. Increasing the frequency asymmetry to $r = 2$ [panels 9(c) and (d)] favors refrigeration by intensifying the spectral response of the strokes, enabling cooling at lower frequencies. The engine regime maintains similar

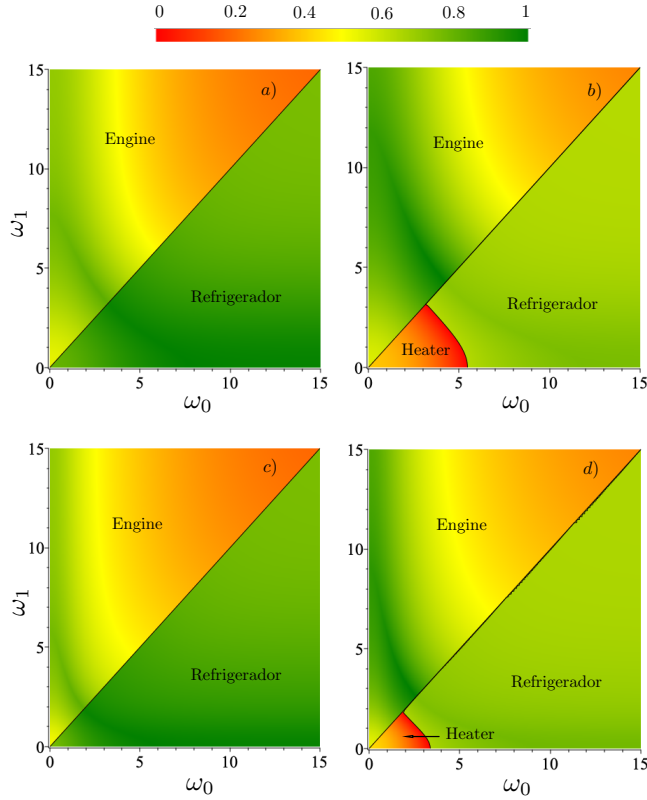


Figure 10. Thermal efficiency of the quantum Stirling cycle in the ω_0 - ω_1 plane. a) $r = 1$, $T_c = 1$, and $T_h = 2$. b) $r = 1$, $T_c = 1$, and $T_h = 3$. c) $r = 2$, $T_c = 1$, and $T_h = 2$. d) $r = 2$, $T_c = 1$, and $T_h = 3$. The parameter g was fixed at $g = 1$.

performance, while the heater mode remains restricted to regions of low efficiency. Under conditions of high r and high T_h [panel 9(d)], the engine efficiency is significantly improved; however, refrigeration becomes limited, demonstrating a more pronounced competition between frequency ratio and thermal gradient.

Overall, without regeneration the performance is strongly limited by the heat dumped into the reservoirs during constant-frequency strokes, enhancing heater behavior and reducing cooling efficiency.

b. With regeneration Figure 10 displays the performance of the Stirling cycle including an ideal regenerator. In this case, heat exchanged during the constant-frequency strokes is internally stored and reused, eliminating an important source of dissipation. For $r = 1$ and $T_h = 2$ [panel 10(a)], the heater mode disappears entirely. High performance is achieved in both engine ($\omega_1 > \omega_0$) and refrigerator ($\omega_1 < \omega_0$) regions, demonstrating that regeneration preserves useful heat fluxes and greatly improves reversibility. When T_h is increased to 3 [panel 10(b)], engine efficiency rises to $\eta \approx 0.8$, while a small frequency heater strip appears due to growing thermal imbalance. Cooling performance slightly decreases but still remains significantly better than without regeneration. Frequency asymmetry enhances these advantages. For $r = 2$ with $T_h = 2$ [panel 10(c)], engine efficien-

cies as high as $\eta \approx 0.9$ are achieved even for relatively small frequencies, and refrigeration is highly efficient for $\omega_1 < \omega_0$. Under both increased r and strong thermal gradient [panel 10(d)], the engine remains the dominant mode with optimal performance, while only a very narrow heater region persists.

In summary, regeneration suppresses dissipation, expands efficient modes, and enables high performance even under asymmetry and strong drive. It is thus the key mechanism that unlocks the full thermodynamic potential of the Raman-coupled working medium.

C. Distinct thermodynamic signatures

The operational-mode diagrams and performance maps reveal robust thermodynamic features that persist across Carnot, Otto, and Stirling cycles. These features are not tied to a specific protocol, but originate from how frequency tuning of the right qubit reshapes the spectrum and controls population redistribution in the Raman-coupled working medium. As a result, similar qualitative patterns emerge across all cycles.

a. Internal heat recovery. The figures show that internal heat management critically determines the accessible operation modes. In the absence of regeneration, regions appear where energy exchange with the reservoirs does not translate into useful work or cooling, leading to accelerator or heater behavior near the boundaries between productive regimes. Introducing a regenerator strongly suppresses these regions by recycling heat exchanged during constant-frequency strokes. This demonstrates that the dominant inefficiencies observed in the maps arise from external dissipation rather than from the spectral structure itself.

b. Performance degradation in extreme regimes. The maps further indicate that extreme parameter regimes degrade thermodynamic performance. Large thermal biases favor irreversible population reshaping, while very small driving frequencies limit the ability of spectral modulation to induce effective energy conversion. In both cases, extended low-performance regions emerge, corresponding to heater-dominated operation. These regimes therefore represent intrinsic limits of frequency-based control, rather than artifacts of a particular cycle.

c. Frequency-driven enhancement. Finally, all figures exhibit extended regions of enhanced performance associated with strong spectral responsiveness to frequency tuning. In these regions, modest frequency variations induce significant population redistribution, enhancing entropy changes along isotherms, work extraction in Otto cycles, and refrigeration performance in Stirling protocols. When regeneration is included, this response-driven mechanism dominates the efficiency maps, as dissipative losses are minimized and the available spectral sensitivity is fully exploited.

Overall, these results show that the thermodynamic

behavior of the Raman-coupled two-qubit machine is governed primarily by population sensitivity to frequency control, rather than by the detailed structure of the cycle. This explains the recurring operational patterns observed across different thermodynamic protocols and highlights frequency tuning as the central organizing principle underlying the reported results.

V. CONCLUSIONS

We have analyzed the thermodynamic performance of a quantum heat machine whose working medium consists of two qubits coupled through a Raman-type exchange interaction. By examining Carnot, Otto, and Stirling operation (with and without regeneration), we mapped in detail the operational modes that emerge when the right-qubit frequency is driven between two values ω_0 and ω_1 . The resulting phase diagrams reveal sharp boundaries separating heat engine, refrigerator, accelerator, and heater behavior, determined by the interplay between frequency asymmetry, Raman mixing, and thermal bias.

In the Carnot cycle, reversible operation is achieved only within a narrow region, close to the optimal frequency ratios. Increasing the temperature gradient broadens the refrigeration domain and restricts engine operation, even though the maximum attainable efficiency rises. The Otto cycle exhibits a richer multimode structure, with all four operational regimes coexisting

over large portions of parameter space. Enhanced spectral asymmetry favors refrigeration, while strong thermal drive improves engine performance but suppresses accelerator behavior.

For the Stirling cycle, the inclusion of a regenerator markedly improves reversibility by internally recycling heat released in the constant-frequency strokes. As a result, heater and accelerator domains are strongly suppressed, and both engine and cooling modes reach near-ideal performance. Under strong coupling and high thermal bias, efficiencies approach $\kappa \approx 0.9$, outperforming the other cycles while remaining robust across a wide range of parameters.

Overall, the Raman-induced level hybridization introduces a controllable left-right asymmetry that enables continuous transitions between distinct thermodynamic behaviors using only frequency tuning. These results demonstrate that Raman-coupled qubit architectures represent highly versatile nanoscale working media, capable of optimized energy conversion in diverse operational regimes and well suited for the design of next-generation quantum thermal machines.

ACKNOWLEDGMENTS

O. R. and M. Rojas thanks CNPq and FAPEMIG for partial financial support. M. Rojas acknowledges CNPq Grant 311565/2025-5.

[1] R. Kosloff, Entropy **15**, 2100 (2013). [I](#)

[2] S. Campbell, et al., Quantum Sci. Technol. **xx**, xxx (2025).

[3] S. Deffner, S. Campbell, *Quantum Thermodynamics: An Introduction to the Thermodynamics of Quantum Information*. Morgan & Claypool Publishers (2019).

[4] F. Binder, L. A. Correa, C. Gogolin, J. Anders, G. Adesso, *Thermodynamics in the Quantum Regime*. (Springer, Cham, 2018), Vol. 195

[5] R. Alicki, J. Phys. A: Math. Gen. **12**, L103 (1979). [I](#)

[6] N. M. Myers, O. Abah, S. Deffner, AVS Quantum Science **4**, 027101 (2022). [I](#)

[7] A. D. Lucio, M. Rojas, C. Filgueiras, Quantum Rep. **7**, 26 (2025). [I](#)

[8] L. M. Cangemi, C. Bhadra, A. Levy, Phys. Rep. **1087**, 1 (2024). [I](#)

[9] J. Roßnagel, S. T. Dawkins, K. N. Tolazzi, O. Abah, E. Lutz, F. Schmidt-Kaler, K. Singer, Science **352**, 325 (2016). [I](#)

[10] Q. Bouton, J. Nettersheim, S. Burgardt, D. Adam, E. Lutz, A. Widera, Nature Communications **12**, 2063 (2021). [I](#)

[11] J. P. S. Peterson, T. B. Batalhão, M. Herrera, A. M. Souza, R. S. Sarthour, I. S. Oliveira, R. M. Serra, Phys. Rev. Lett. **123**, 240601 (2019). [I](#)

[12] M. Josefsson, A. Svilans, A. M. Burke, E. A. Hoffmann, S. Fahlvik, C. Thelander, M. Leijnse, H. Linke, Nature Nanotech. **13**, 920 (2018). [I](#)

[13] J. P. Pekola, Nature Phys. **11**, 118 (2015). [I](#)

[14] G. Marchegiani, P. Virtanen, F. Giazotto, M. Campisi, Phys. Rev. Appl. **6**, 054014 (2016). [I](#)

[15] F. Giazotto, M. J. Martínez-Pérez, Nature **492**, 401 (2012). [I](#)

[16] K. Zhang, F. Barini, P. Meystre, Phys. Rev. Lett. **112**, 150602 (2014). [I](#)

[17] A. Dechant, N. Kiesel, E. Lutz, Phys. Rev. Lett. **114**, 183602 (2015). [I](#)

[18] P. P. Hoffer, M. Perarnau-Lloblet, J. B. Brask, R. Silva, M. Huber, N. Brunner, Phys. Rev. B **94**, 235420 (2016). [I](#)

[19] A. U. C. Hardal, N. Aslan, C. M. Wilson, O. E. Mustecaplioglu, F. Schmidt-Kaler, K. Singer, Science **352**, 325 (2016). [I](#)

[20] J. -Z. He, X. He, J. Zheng, Chinese Phys. B **21**, 50303 (2012). [I](#)

[21] E. Albayrak, Int. J. Quantum Inf. **11**, 1350021 (2013).

[22] M. Asadian, S. Ahadpour, F. Mirmasoudi, Sci. Rep. **12**, 7081 (2022).

[23] E. I. Kuznetsova, M. A. Yurishev, S. Haddadi, Quantum Inf. Process. **22**, 192 (2023). [I](#)

[24] J. -Z. He, X. He, J. Zheng, Int. J. Theor. Phys. **51**, 2066 (2012). [I](#)

[25] O. Rojas, M. Rojas, Ann. Phys. (Berlin) **537**, 2400291 (2025). [II D](#)

- [26] O. Rojas, M. Rojas, S. M. de Souza, Phys. Rev. E **111**, 044121 (2025).
- [27] J. L. D. de Oliveira, M. Rojas, C. Filgueiras, Phys. Rev. E **104**, 014149 (2021). [I](#)
- [28] E. M. Centamori, M. Campisi, V. Giovannetti, Sci. Post Phys. **18**, 160 (2025). [I](#)
- [29] G. Piccitto, M. Campisi, D. Rossini, New. J. Phys. **24**, 103023 (2025). [I](#)
- [30] X. -L. Huang, X. -Y. Niu, X. -M. Xiu, X. -X. Yi, Eur. Phys. J. D **68**, 32 (2014). [I](#)
- [31] C. Araya, F. J. Peña, A. Norambuena, B. Castorene, P. Vargas, Technologies **11**, 169 (2023).
- [32] A. H. B. Pili, R. Khordad, H. R. R. Sedehi, A. Avazpour, Int. J. Theor. Phys. **62**, 192 (2023).
- [33] H. R. Rastegar-Sedehi, C. Cruz, Front. Phys. **13**, 1512998 (2025).
- [34] Y. Ying, L. Chen, F. Wu, Y. Ge, Physica A **547**, 123856 (2020).
- [35] Y.-S. Wang, M.-H. Yung, D. Xu, M. Liu, X. Chen, Phys. Rev. A **109**, 022208 (2024).
- [36] H-R. Rastegar-Sedehi, N. Papadatos, C. Cruz, Eur. Phys. J. Plus **140**, 199 (2025). [I](#)
- [37] A. H. B. Pili, R. Khordad, H. R. R. Sedehi, A. Avazpour, Int. J. Theor. Phys. **62**, 192 (2023). [I](#)
- [38] S. Çakmak, H. R. Rastegar Sedehi, Phys. Scr. **98**, 105921 (2023).
- [39] C. Cruz, H. -R. Rastegar-Sedehi, M. F. Anka, T. R. de Oliveira, M. Reis, Quantum Sci. Technol. **8**, 035010 (2023). [I](#)
- [40] M. H. B. Chakour, A. E. Allati, Y. Hassouni, Eur. Phys. J. D **75**, 42 (2021). [I](#)
- [41] A. H. B. Pili, R. Khordad, H. R. R. Sedehi, Eur. Phys. J. Plus **138**, 871 (2023). [I](#)
- [42] C. Kargi, M. T. Naseem, T. Opatrny, O. E. Musterplioglu, G. Kurizhi, Phys. Rev. E **99**, 042121 (2019). [I](#), [II](#)